



HAL
open science

Cry11Aa and Cyt1Aa exhibit different structural orders in crystal topography

Shu-wen W. Chen, Jean-marie Teulon, Jean-luc Pellequer

► **To cite this version:**

Shu-wen W. Chen, Jean-marie Teulon, Jean-luc Pellequer. Cry11Aa and Cyt1Aa exhibit different structural orders in crystal topography. *Journal of Molecular Recognition*, 2023, 36 (9), pp.e3047. 10.1002/jmr.3047 . hal-04208522

HAL Id: hal-04208522

<https://hal.science/hal-04208522>

Submitted on 15 Sep 2023

HAL is a multi-disciplinary open access archive for the deposit and dissemination of scientific research documents, whether they are published or not. The documents may come from teaching and research institutions in France or abroad, or from public or private research centers.

L'archive ouverte pluridisciplinaire **HAL**, est destinée au dépôt et à la diffusion de documents scientifiques de niveau recherche, publiés ou non, émanant des établissements d'enseignement et de recherche français ou étrangers, des laboratoires publics ou privés.

RESEARCH ARTICLE

Cry11Aa and Cyt1Aa exhibit different structural orders in crystal topography

Shu-wen W. Chen^{1,2}  | Jean-Marie Teulon¹ | Jean-Luc Pellequer¹ 

¹Univ. Grenoble Alpes, CEA, CNRS, Institut de Biologie Structurale (IBS), Grenoble, France

²Rue Cyprien Jullin, Vinay, France

Correspondence

Shu-wen W. Chen and Jean-Luc Pellequer, Univ. Grenoble Alpes, CEA, CNRS, Institut de Biologie Structurale (IBS), F-38000 Grenoble, France.

Email: cmft551@yahoo.com and jean-luc.pellequer@ibs.fr

Abstract

Cry11Aa and Cyt1Aa are two pesticidal toxins produced by *Bacillus thuringiensis* subsp. *israelensis*. To improve our understanding of the nature of their oligomers in the toxic actions and synergistic effects, we performed the atomic force microscopy to probe the surfaces of their natively grown crystals, and used the L-weight filter to enhance the structural features. By L-weight filtering, molecular sizes of the Cry11Aa and Cyt1Aa monomers obtained are in excellent agreement with the three-dimensional structures determined by x-ray crystallography. Moreover, our results show that the layered feature of a structural element distinguishes the topographic characteristics of Cry11Aa and Cyt1Aa crystals, suggesting that the Cry11Aa toxin has a better chance than Cyt1Aa for multimerization and therefore cooperativeness of the toxic actions.

KEYWORDS

AFM, Bti, crystal protein, high-resolution imaging, insecticidal toxin, L-weight filter, protoxin

Bacillus thuringiensis subsp. *israelensis* (Bti) has appealed a great deal of attention for its importance in biological control against mosquitoes and blackflies.^{1,2} The toxin lyses erythrocytes and is toxic to mice as well.³ The toxicity of Bti resides in its parasporal inclusions where four major insecticidal proteins Cry11Aa, Cry4A, Cry4B, and Cyt1A were found.⁴ Among the four, Cry11Aa, previously called CryIVD, is most toxic, yielding the lowest value of lethal concentration (LC₅₀).⁵ Nevertheless, the Cry11Aa knockout Bti still exhibited variable degrees of toxic effects on different mosquito species.⁶ In the parasporal inclusions, Cry11Aa is a 70-kDa protoxin activated by proteolytic processing to generate the N- and C-terminal fragments (36 and 32 kDa), which remain associated and retain toxicity to insects.⁷ Cyt1Aa is 27 kDa protein that belongs to a family called the cytolytic (Cyt) toxin, whereas Cry11Aa is a member of one of the crystalline (Cry) toxin families.⁸

Cry11Aa is a three-domain toxins, characterized by three structural domains responsible for receptor binding and membrane insertion.^{9–11} However, the domain-function relationship is not so strict, some Cry toxins targeted the receptor of larval midgut cells by different domains.¹² The binding of Cry toxins to various specific

receptors was therefore exploited as to differentiate the toxicity extent.¹³ Moreover, swapping of domain III occurred among Cry toxins in evolutionary paths, resulting in the diversity of the toxin family.¹¹ In pore formation, the Cry crystal proteins were proposed to interact sequentially with several membrane receptors, inducing the oligomerization and membrane insertion.⁸ Based on a molecular model of Cry11Aa using the crystal structure of Cry2Aa (PDB code 1I5P),¹⁴ a loop epitope of domain II (protein sequence 257–268) was identified in interaction with membrane receptors of *Aedes aegypti* midgut cells.¹⁵

Toxicity synergism is observed between Cry11Aa and Cyt1Aa.^{16,17} The reduction of mosquito resistance to Cry11Aa with the presence of Cyt1Aa provides a molecular genetic strategy for transgenic plants and bacterial insecticides.¹⁸ To understand the molecular mechanisms of the synergistic toxicity of Cry11Aa and Cyt1Aa, many efforts of genetic engineering were made such as single-point to triple mutations on Cyt1Aa protein residues^{19,20} or analyzing the three-dimensional (3D) structure of both toxins for identification of specific binding sites in either toxins or membranes of

This is an open access article under the terms of the [Creative Commons Attribution-NonCommercial](https://creativecommons.org/licenses/by-nc/4.0/) License, which permits use, distribution and reproduction in any medium, provided the original work is properly cited and is not used for commercial purposes.

© 2023 The Authors. *Journal of Molecular Recognition* published by John Wiley & Sons Ltd.

host cells. Cyt1Aa was shown to act as a receptor in the membrane for Cry11Aa to bind specifically.²¹ By anchoring Cry11Aa onto the membrane surface, it promotes the oligomerization of Cry11Aa, which is required prior to pore formation in the membrane.²²

Atomic force microscopy (AFM) has been widely applied to visualizations of the distribution and multimerization of Cry and Cyt toxins from various Bt subspecies interacting with different membrane systems.^{23–28} As described above, the two proteolytically cleaved Cry11Aa fragments remain associated,⁷ and thus, the 3D structure of active Cry11Aa must resemble the crystal structure of the protoxin.²⁶ Since multimerization of Cry11Aa molecules is a key process for its toxic activity,²² the native association of Cry11Aa monomers in crystal is likely most representable for the nature of the protein assembled in the process of toxic actions. Despite the 3D crystal structure of Cry11Aa (or Cyt1Aa) protoxin has been determined,^{26,28} the molecular arrangement of the protein crystal subjective to the native growth is difficult for visual perception of the lattice pattern of crystal cell units. To shed light on the molecular arrangement of Cry11Aa crystal as well as Cyt1Aa grown natively, we employed the AFM imaging to visualize topographic structures of these two protoxin crystals.

1 | METHODOLOGY

1.1 | AFM imaging and L-weight filter

One major obstacle to visualize the detail of surface structures of materials in an AFM image is that the intensity variation is too minute, relative to the global contrast, to be perceived by the human eye.²⁹ Consequently, the topographic information of molecular structure is either ignored or disregarded, leading to misdiagnosis of image contents or un-optimized AFM instrumentation. Even worse, the usefulness of this handy imaging technology is totally undervalued. Notwithstanding, this type of impediment can be alleviated by appropriate post-processing, which is essential for “single-image analysis” on AFM topographs at high resolution³⁰ when multi-image averaging is unrealistic for improving the image quality.

L-weight filter has been proved as a powerful processing tool for AFM molecular images for the studies of estimation of molecular size of an anonymized protein²⁹ to DNA-HU protein binding reaction,³¹ and from fibrillation of cytosolic abundant heat-soluble proteins from tardigrades³² to the deposition of bacteriorhodopsin with lipid membranes on mica.³³ It has a similar function as the well-known Laplacian mask³⁴ to sharpen the boundary of the image object, and substantially diminishes severe broadening effects brought by the AFM probing tip. It has also been implicitly implemented in the DeStripe program for removing striping noise.³⁵ The outcome format of the L-weight filtered image is expressed as $I(x, y) \times \Delta \hat{I}(x, y)$ with the intensity value $I(x, y)$ at pixel (x, y) and the normalized value of offset Laplacian function $\Delta \hat{I}(x, y)$.^{29,31} In order to modulate the fluctuating amplitudes of $\Delta \hat{I}(x, y)$ data values, a 2D-isotropic Gaussian smoothing window³⁴ was implemented; the window size $2w + 1$ and the Gaussian spread σ are tunable in order to obtain a desirable sharpness for topographic features. The processing effect of this filter can be further enhanced by repetitive use. The processed image

still keeps some sense of topographic height, unlike the micrographs acquired by TEM (transmission electron microscopy) which are flat.

1.2 | AFM Instrumental setups and data acquisition

The objects to be imaged are Cyt1Aa and Cry11Aa protoxin crystals. Purified crystals were conserved in ultrapure water. AFM imaging was performed using the PeakForce tapping mode of Multimode 8 AFM (Bruker, Santa Barbara, CA) equipped with a Nanoscope V controller. A semi-automated scanasyst mode was used with a classical ramp of 150 nm while the set point was manually controlled. ScanAsyst-Air HR cantilever for Cry11Aa and SNL cantilever for Cyt1Aa were used (Bruker AFM probes, Camarillo, CA) with a scanning rate of ~ 1.0 Hz. All measurements have been performed in air. The original AFM images, by default, are the raw image pre-treated by the Gwyddion software³⁶ as described elsewhere.³⁷ Length measurements were extracted with the profile along an arbitrary line tool of Gwyddion.³⁶ The corresponding histograms were tabulated using GraphPad Prism 5.

2 | RESULTS

The AFM topography of a Cry11Aa bulky crystal is shown in Figure 1A; the size was estimated as about $0.93 \times 0.50 \times 0.15 \mu\text{m}^3$ with an appearance of a very bright solid object and non-convex geometry. Owing to the high contrast of the crystal object against the background, one may tune the range of intensity display for gaining some structural features from the AFM image. Elevating the minimal intensity displayed in Figure 1A almost to the half of the maximal value, Figure 1B reveals vaguely the stacking sequence of layer-like structures which progressively shrink to give the final shape of the crystal. The height difference between adjacent layers was estimated as 6.6 ± 0.9 nm based on the original topography. Distribution of values is shown in Figure 1G. The visibility of the layered structure in (A) can be further enhanced by applying the L-weight filter, shown in Figure 1C. It becomes evident that the structure of these layer-like elements resembles a latticework. The same structural feature appeared in other Cry11Aa crystals with different sizes and shapes, indicating that the feature of the latticed layer is a characteristic of native Cry11Aa crystal surface. This structural element of shorter-length scale implies that fewer toxin molecules are required to initiate multimerization. As known, the protein multimerization provokes a high-concentration mimicry locally, in turn, it promotes the biological activity of the protein.³⁸ With the aid of the L-weight filter, AFM imaging reveals that Cry11Aa crystal exhibits a hierarchical order³⁹ of surface structure on different size (length) scales, as revealed in Figure 1D,E.

To better view the structure, Figure 1F is a higher-resolution scanning over a subimage of Figure 1A processed by the L-weight filter and numerically magnified ($\times 2$), wherein a layer structural element was marked by several profile lines to indicate the filamentous ridges formed of connected protein monomers. The interval distance of two adjacent ridges (oriented according to the yellow line in Figure 1F) was estimated

from the processed images as 15.5 ± 1.1 nm (a sampling number of 37). Analyzing the profile of intensities over the filamentous ridges (oriented according to the white line in Figure 1F), we obtained a width of 15.5

± 4.1 nm for the protruding sub-structures along the ridges (with a sampling number of 40). Values obtained from all these profiles are assembled in distribution plots (Figure 1G). Taken together, the size of

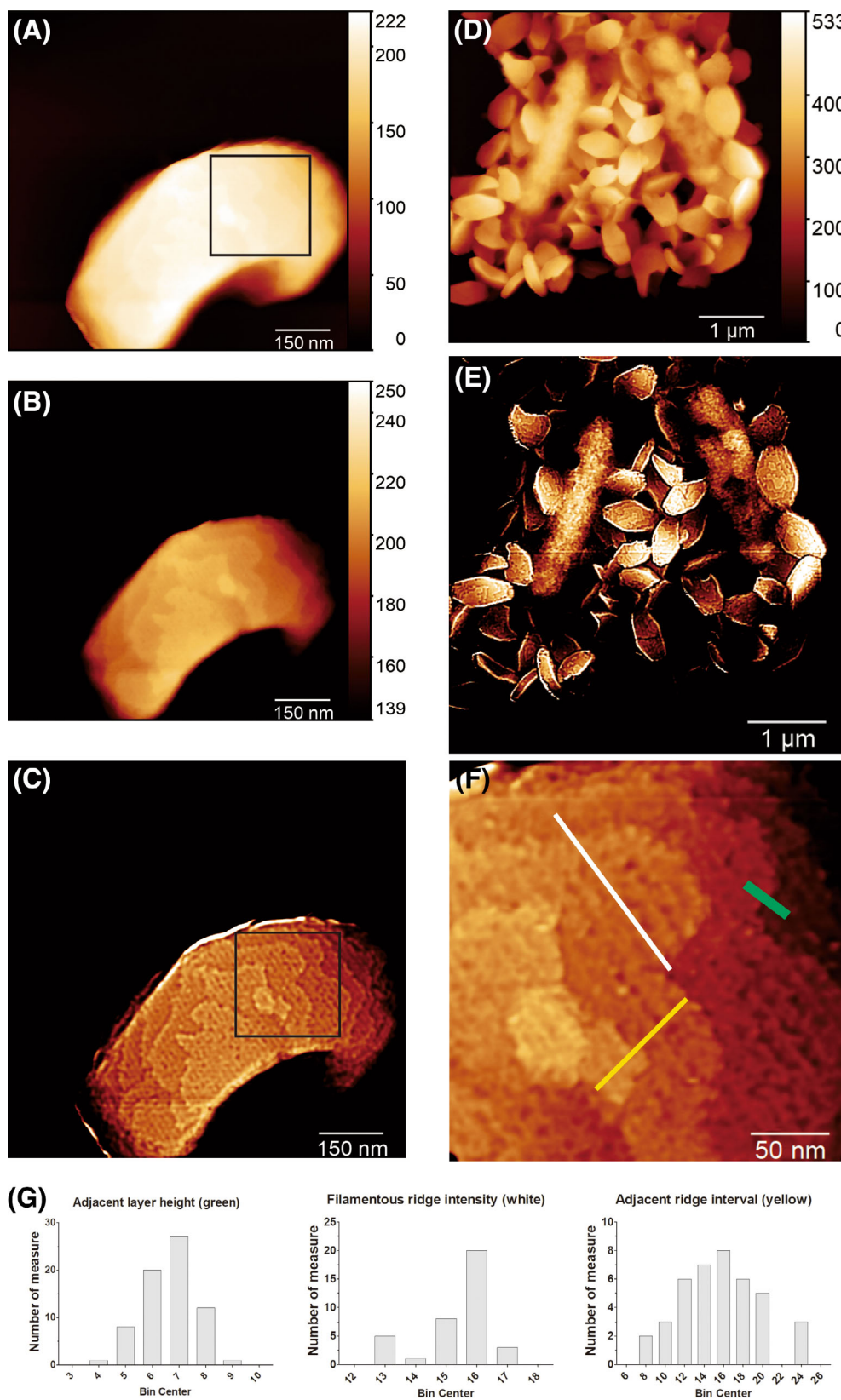


FIGURE 1 Legend on next page.

Cry11Aa monomers was estimated as $(15.5 \pm 1.1) \times (15.5 \pm 4.1) \text{ nm}^2$, which is very close to that obtained from the 3D crystal structure, $6 \times 16 \times 17 \text{ nm}^3$, by the x-ray crystallography.²⁶

Apart from Cry11Aa, the results of AFM imaging on Cyt1Aa protoxin crystals are presented in Figure 2A, and the L-weight filtered (A) was dissected into three parts illustrated in Figure 2B–D. From

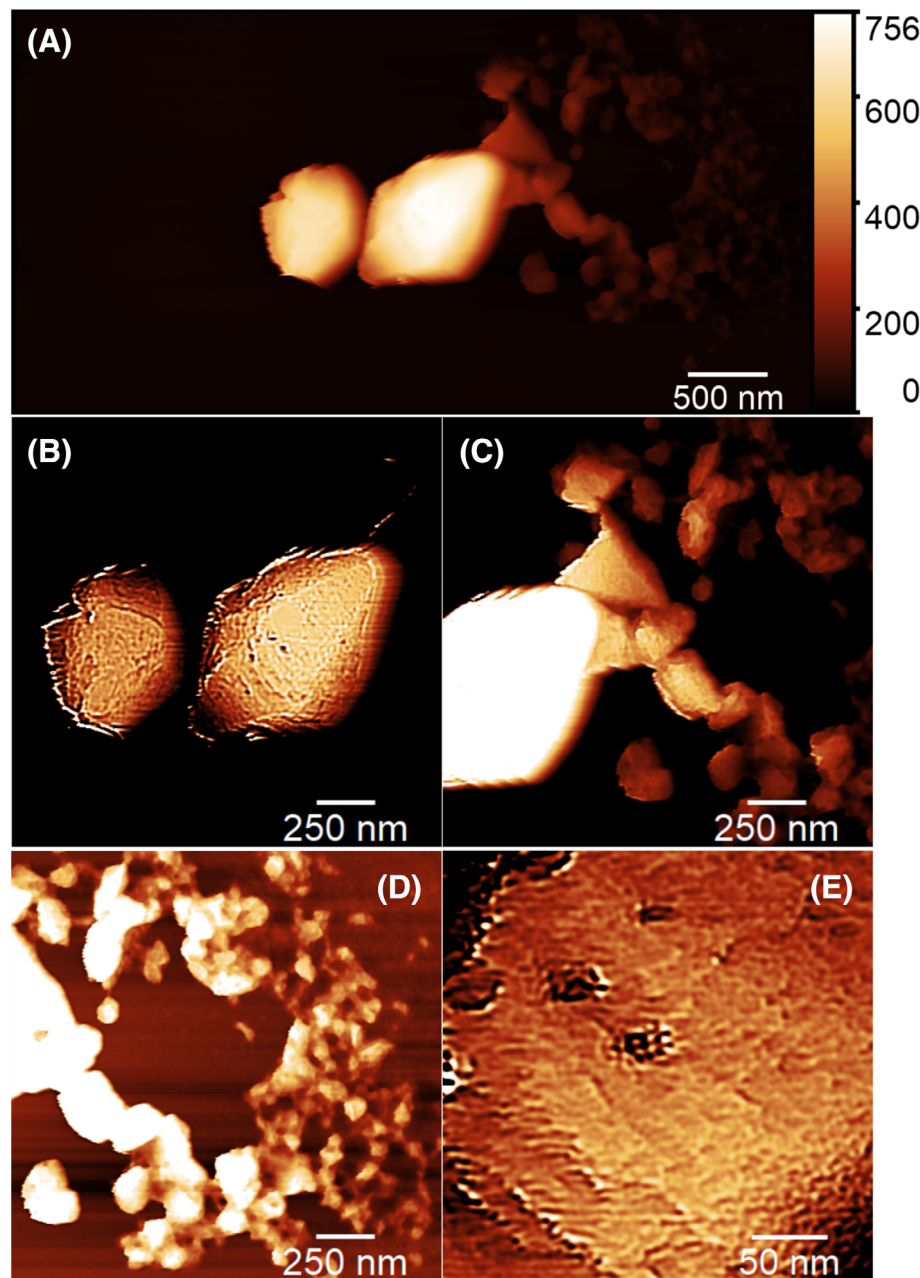


FIGURE 2 (A) Atomic force microscopy (AFM) topography of crystalline Cyt1Aa protoxin. The image is composed of 1024×512 pixels with a physical dimension of $4.98 \times 2.49 \mu\text{m}^2$ in a full range of height display of 0–0.8 μm ; alongside is the z-scale bar. (B–D) Three dissected (or cropped) sub-images, somewhat overlapped for tracing the disposition of those crystal particles, from the processed image of (A) by four times of the L-weight filter. The size of smoothing window for the filter is $2 \times 2 + 1$ pixels with $\sigma = 1.03$ pixels (see Figure 1). Each dissected image is formed of 370×370 pixels (i.e., $1.8 \times 1.8 \mu\text{m}^2$) and displayed at different intensity ranges for better visualization of the objects dispersed in the full image. The dissection starts with the two large bipyramid-like crystals and then reaches the left border of the full image. (E) Magnified the local area of image (B) indicated by the black arrow. With $\times 3.32$ magnification, image (E) is composed of 380×380 pixels with a physical dimension of $278.3 \times 278.3 \text{ nm}^2$. Several holes are visible on the surface.

FIGURE 1 (A) Atomic force microscopy (AFM) topography of crystalline Cry11Aa protoxin acquired at the probing resolution of 0.98 nm per pixel. The image is composed of 1024×1024 pixels in a full range of height display, 0–222 nm with the z-scale bar in the unit of nanometer. (B) Image (A) presented in a narrowed intensity range, 139–250 nm, for increasing the visibility of image content. (C) Image (A) processed by the L-weight filter. The L-weight filter was consecutively applied twice; the smoothing parameters $w = 12$ and $\sigma = 4.06$ pixels (see Section 1.1). The black square in the image is corresponding to that in (A). (D) AFM imaging on Cry11Aa crystals of various sizes and shapes. The image is composed of 512×512 pixels in a physical dimension of $5 \times 5 \mu\text{m}^2$. The z-scale color bar is up to 0.5 μm . (E) The processed image of (D) by the L-weight filter; see parameterization details in (C). The L-weight filter was consecutively used two times with $w = 1$ and $\sigma = 1.02$ pixels. (F) The AFM magnified and subsequently processed image of the black-outlined region in (A). The image consists of 380×380 pixels with a pixel width of 0.55 nm. Note that L-weight filtered images lose the true meaning of physical height; therefore, the z-scale color bars are not presented. (G) Distribution of extracted lengths from unprocessed (A) and processed (F) AFM images. The left panel is the adjacent layer height (green mark on F) that is obtained on the unprocessed image (A). The middle panel is the filamentous ridge intensity that corresponds to measurements along the white direction (white line on F), the right panel is the adjacent ridge interval that corresponds to measurements obtained in the yellow direction (yellow line on F).

these divided subimages, Cyt1Aa exhibits a variety of particle sizes and shapes. Figure 2C,D displays Cyt1Aa protoxin that forms smaller clustered particles, whereas Figure 2B aims to reveal the two largest Cyt1Aa crystals of bipyrmaid-like shape. The size of the largest crystal (on the right in Figure 2B) was estimated as $0.74 \times 1.1 \times 0.85 \mu\text{m}^3$, while that of the protein monomer is estimated using vertical profiles mapped with the processed image (Figure 2E) as $(6.7 \pm 0.9) \times (6.9 \pm 1.7) \text{nm}^2$ (a sampling number of 16 and 19, respectively), which is in good agreement with the observation from the 3D crystal structure ($6 \times 6 \times 16 \text{nm}^3$).²⁸ The surface features of Cyt1Aa are less discernible with further magnification, as shown in Figure 2E, owing to a much lower probing resolution. Nevertheless, it is obvious that Cyt1Aa lacks the layered substructure in the crystal topography compared to Cry11Aa, which hinders the estimation of the vertical dimension of the protein monomer. The clustered solid particles shown in Figure 2D infer that Cyt1Aa tends to aggregate at low numbers of toxin molecules, as displayed elsewhere.²⁸ The rise of two distinct molecular mechanisms regarding the Cyt1Aa toxicity, the pore formation⁴⁰ and detergent-like models,^{41,42} probably reflects the process of increasing toxin molecules in interaction with the membrane.

Although Cry11Aa and Cyt1Aa are both structurally classified as a Cry solid, their monomeric molecules do not follow exactly the periodicity while exhibiting some disorders locally over all the crystal. Analogous to the definitions of structural orders for characterizing amorphous solids,⁴³ Cry11Aa crystal renders itself as the largest structural element with the highest hierarchical order 3; the layer-like structures are of order 2 with local dimensionality of 2 to stack up the 3D crystal, wherein the filamentous ridges are of order 1. The present results show fewer structural hierarchical orders for Cyt1Aa than for Cry11Aa, suggesting the structural orders 2 and 1 of Cry11Aa are closely related to multimerization and molecular mechanisms in synergistic toxicity in specific interaction with Cyt1Aa-membrane complexes.

3 | CONCLUSION

The present results have shown that Cry11Aa protoxin exhibits a layered substructure in the crystal topography while Cyt1Aa lacks such a surface characteristic. Although Cry11Aa and Cyt1Aa are both in Cry forms, their translational and orientational orders are not perfectly organized in a definite lattice pattern, leading to various sizes and shapes as well as structural features. In solution, the monomers of Cry11Aa or Cyt1Aa move freely and disorderedly. Once anchored onto a membrane surface, the development of molecular assembly will depend on the networking forces underlying the surface structures of Cry11Aa and Cyt1Aa crystals and the synergistic toxicity. Combining with the L-weight filter, this work has demonstrated the power of AFM in imaging on arbitrary shapes of solid objects to reveal the molecular architecture. Together with our previous experiences, AFM imaging with the L-weight filter has been shown to be extremely useful for acquiring high-resolution information of biomolecular systems from solution to solid state.

AUTHOR CONTRIBUTIONS

Shu-wen W. Chen designed and performed image processing. Jean-Marie Teulon acquired AFM images. Shu-wen W. Chen and Jean-Luc Pellequer wrote the manuscript.

ACKNOWLEDGMENTS

IBS acknowledges integration into the Interdisciplinary Research Institute of Grenoble (IRIG, CEA). This work acknowledges the AFM platform at the IBS. We acknowledge Guillaume Tetreau, Elena A. Andreeva, and Anne-Sophie Banneville for producing and preparing *Bacillus* crystals. We thank Jacques-Philippe Colletier for initiating the Bti project and for providing the crystals.

CONFLICT OF INTEREST STATEMENT

The authors declare no conflicts of interest.

DATA AVAILABILITY STATEMENT

The data that support the findings of this study are available from the corresponding author upon reasonable request.

ORCID

Shu-wen W. Chen  <https://orcid.org/0000-0003-4205-4931>

Jean-Luc Pellequer  <https://orcid.org/0000-0002-8944-2715>

REFERENCES

- Goldberg LJ, Margalit J. A bacterial spore demonstrating rapid larvicidal activity against *Anopheles sergentii*, *Uranotaenia unguiculata*, *Culex univittatus*, *Aedes aegypti* and *Culex pipiens*. *Mosq News*. 1977; 37:355-358.
- De Barjac H. Une nouvelle variété de *Bacillus thuringiensis* très toxique pour les moustiques: *Bacillus thuringiensis* var *israelensis* sérotype 14. *CR Hebd Seances Acad Sci Ser D Sci Nat*. 1978;286:797-800.
- Armstrong JL, Rohrmann GF, Beaudreau GS. Delta endotoxin of *Bacillus thuringiensis* subsp. *israelensis*. *J Bacteriol*. 1985;161:39-46. doi:10.1128/jb.161.1.39-46.1985
- Chilcott CN, Ellar DJ. Comparative toxicity of *Bacillus thuringiensis* var. *israelensis* crystal proteins in vivo and in vitro. *J Gen Microbiol*. 1988; 134:2551-2558. doi:10.1099/00221287-134-9-2551
- Crickmore N, Bone EJ, Williams JA, Ellar DJ. Contribution of the individual components of the delta-endotoxin crystal to the mosquitocidal activity of *Bacillus thuringiensis* subsp. *israelensis*. *FEMS Microbiol Lett*. 1995;131:249-254. doi:10.1111/j.1574-6968.1995.tb07784.x
- Poncet S, Anello G, Delecluse A, Klier A, Rapoport G. Role of the CryIVD polypeptide in the overall toxicity of *Bacillus thuringiensis* subsp. *israelensis*. *Appl Environ Microbiol*. 1993;59:3928-3930. doi:10.1128/AEM.59.11.3928-3930.1993
- Dai S-M, Gill SS. In vitro and in vivo proteolysis of the *Bacillus thuringiensis* subsp. *israelensis* CryIVD protein by *Culex quinquefasciatus* larval midgut proteases. *Insect Biochem Mol Biol*. 1993;23:273-283. doi:10.1016/0965-1748(93)90008-G
- Soberón M, Pardo L, Muñoz-Garay C, et al. Pore formation by Cry toxins. *Adv Exp Med Biol*. 2010;677:127-142. doi:10.1007/978-1-4419-6327-7_11
- Schnepf E, Crickmore N, Van Rie J, et al. *Bacillus thuringiensis* and its pesticidal crystal proteins. *Microbiol Mol Biol Rev*. 1998;62:775-806. doi:10.1128/mmlr.62.3.775-806.1998
- Adang MJ, Crickmore N, Jurat-Fuentes JL. Diversity of *Bacillus thuringiensis* crystal toxins and mechanism of action. *Advances in Insect Physiology*. 1st ed. Academic Press; 2014:39-87.

11. Bravo A, Gill SS, Soberon M. Mode of action of *Bacillus thuringiensis* Cry and Cyt toxins and their potential for insect control. *Toxicon*. 2007;49:423-435. doi:10.1016/j.toxicon.2006.11.022
12. Dechkla M, Charoenjotivadhanakul S, Imtong C, Visitsattapongse S, Li HC, Angsuthanasombat C. Cry4Aa and Cry4Ba mosquito-active toxins utilize different domains in binding to a particular *Culex* ALP isoform: a functional toxin receptor implicating differential actions on target larvae. *Toxins*. 2022;14:14. doi:10.3390/toxins14100652
13. Likitvatanavong S, Chen J, Evans AM, Bravo A, Soberon M, Gill SS. Multiple receptors as targets of Cry toxins in mosquitoes. *J Agric Food Chem*. 2011;59:2829-2838. doi:10.1021/jf1036189
14. Morse RJ, Yamamoto T, Stroud RM. Structure of Cry2Aa suggests an unexpected receptor binding epitope. *Structure*. 2001;9:409-417. doi:10.1016/s0969-2126(01)00601-3
15. Fernandez LE, Perez C, Segovia L, et al. Cry11Aa toxin from *Bacillus thuringiensis* binds its receptor in *Aedes aegypti* mosquito larvae through loop alpha-8 of domain II. *FEBS Lett*. 2005;579:3508-3514. doi:10.1016/j.febslet.2005.05.032
16. Wu D, Chang FN. Synergism in mosquitocidal activity of 26 and 65 kDa proteins from *Bacillus thuringiensis* subsp. *israelensis* crystal. *FEBS Lett*. 1985;190:232-236. doi:10.1016/0014-5793(85)81290-4
17. Chang C, Yu YM, Dai SM, Law SK, Gill SS. High-level cryIVD and cytA gene expression in *Bacillus thuringiensis* does not require the 20-kilodalton protein, and the coexpressed gene products are synergistic in their toxicity to mosquitoes. *Appl Environ Microbiol*. 1993;59:815-821. doi:10.1128/AEM.59.3.815-821.1993
18. Wirth MC, Georghiou GP, Federici BA. CytA enables CryIV endotoxins of *Bacillus thuringiensis* to overcome high levels of CryIV resistance in the mosquito, *Culex quinquefasciatus*. *Proc Natl Acad Sci U S A*. 1997;94:10536-10540. doi:10.1073/pnas.94.20.10536
19. Ward ES, Ellar DJ, Chilcott CN. Single amino acid changes in the *Bacillus thuringiensis* var. *israelensis* delta-endotoxin affect the toxicity and expression of the protein. *J Mol Biol*. 1988;202:527-535. doi:10.1016/0022-2836(88)90283-5
20. Onofre J, Pacheco S, Torres-Quintero MC, Gill SS, Soberon M, Bravo A. The Cyt1Aa toxin from *Bacillus thuringiensis* inserts into target membranes via different mechanisms in insects, red blood cells, and lipid liposomes. *J Biol Chem*. 2020;295:9606-9617. doi:10.1074/jbc.RA120.013869
21. Perez C, Fernandez LE, Sun J, et al. *Bacillus thuringiensis* subsp. *israelensis* Cyt1Aa synergizes Cry11Aa toxin by functioning as a membrane-bound receptor. *Proc Natl Acad Sci U S A*. 2005;102:18303-18308. doi:10.1073/pnas.0505494102
22. Munoz-Garay C, Rodriguez-Almazan C, Aguilar JN, et al. Oligomerization of Cry11Aa from *Bacillus thuringiensis* has an important role in toxicity against *Aedes aegypti*. *Appl Environ Microbiol*. 2009;75:7548-7550. doi:10.1128/AEM.01303-09
23. Vie V, Van Mau N, Pomarede P, et al. Lipid-induced pore formation of the *Bacillus thuringiensis* Cry1Aa insecticidal toxin. *J Membr Biol*. 2001;180:195-203. doi:10.1007/s002320010070
24. Puntheeranurak T, Stroh C, Zhu R, Angsuthanasombat C, Hinterdorfer P. Structure and distribution of the *Bacillus thuringiensis* Cry4Ba toxin in lipid membranes. *Ultramicroscopy*. 2005;105:115-124. doi:10.1016/j.ultramic.2005.06.026
25. Laflamme E, Badia A, Lafleur M, Schwartz JL, Laprade R. Atomic force microscopy imaging of *Bacillus thuringiensis* Cry1 toxins interacting with insect midgut apical membranes. *J Membr Biol*. 2008;222:127-139. doi:10.1007/s00232-008-9106-8
26. Tetreau G, Sawaya MR, De Zitter E, et al. De novo determination of mosquitocidal Cry11Aa and Cry11Ba structures from naturally-occurring nanocrystals. *Nat Commun*. 2022;13:4376. doi:10.1038/s41467-022-31746-x
27. Tharad S, Toca-Herrera JL, Promdonkoy B, Krittanai C. *Bacillus thuringiensis* Cyt2Aa2 toxin disrupts cell membranes by forming large protein aggregates. *Biosci Rep*. 2016;36:36. doi:10.1042/BSR20160090
28. Tetreau G, Banneville AS, Andreeva EA, et al. Serial femtosecond crystallography on in vivo-grown crystals drives elucidation of mosquitocidal Cyt1Aa bioactivation cascade. *Nat Commun*. 2020;11:1153. doi:10.1038/s41467-020-14894-w
29. Chen S-wW, Teulon J-M, Godon C, Pellequer J-L. Atomic force microscope, molecular imaging, and analysis. *J Mol Recognit*. 2016;29:51-55. doi:10.1002/jmr.2491
30. Chen S-wW, Odorico M, Meillan M, et al. Nanoscale structural features determined by AFM for single virus particles. *Nanoscale*. 2013;5:10877-10886. doi:10.1039/C3NR02706F
31. Chen S-wW, Banneville AS, Teulon JM, Timmins J, Pellequer JL. Nanoscale surface structures of DNA bound to *Deinococcus radiodurans* HU unveiled by atomic force microscopy. *Nanoscale*. 2020;12:22628-22638. doi:10.1039/d0nr05320a
32. Malki A, Teulon JM, Camacho-Zarco AR, et al. Intrinsically disordered tardigrade proteins self-assemble into fibrous gels in response to environmental stress. *Angew Chem Int Ed Engl*. 2022;61:e202109961. doi:10.1002/anie.202109961
33. Mukhina T, Gerelli Y, Hemmerle A, et al. Insertion and activation of functional bacteriorhodopsin in a floating bilayer. *J Colloid Interface Sci*. 2021;597:370-382. doi:10.1016/j.jcis.2021.03.155
34. Gonzalez RC, Woods RE. *Digital Image Processing*. 3rd ed. Pearson Education Inc; 2008.
35. Chen S-wW, Pellequer JL. DeStripe: frequency-based algorithm for removing stripe noises from AFM images. *BMC Struct Biol*. 2011;11:7. doi:10.1186/1472-6807-11-7
36. Nečas D, Klapetek P. Gwyddion: an open-source software for SPM data analysis. *Centr Eur J Phys*. 2012;10:181-188. doi:10.2478/s11534-011-0096-2
37. Teulon J-M, Godon C, Chantalat L, et al. On the operational aspects of measuring nanoparticle sizes. *Nanomaterials*. 2019;9:18. doi:10.3390/nano9010018
38. McGhee JD, von Hippel PH. Theoretical aspects of DNA-protein interactions: co-operative and non-co-operative binding of large ligands to a one-dimensional homogeneous lattice. *J Mol Biol*. 1974;86:469-489. doi:10.1016/0022-2836(74)90031-x
39. Lakes R. Materials with structural hierarchy. *Nature*. 1993;361:511-515. doi:10.1038/361511a0
40. Knowles BH, Ellar DJ. Colloid-osmotic lysis is a general feature of the mechanism of action of *Bacillus thuringiensis* delta-endotoxins with different insect specificity. *Biochim Biophys Acta*. 1987;924:509-518. doi:10.1016/0304-4165(87)90167-X
41. Thomas WE, Ellar DJ. Mechanism of action of *Bacillus thuringiensis* var *israelensis* insecticidal delta-endotoxin. *FEBS Lett*. 1983;154:362-368. doi:10.1016/0014-5793(83)80183-5
42. Manceva SD, Pusztai-Carey M, Russo PS, Butko P. A detergent-like mechanism of action of the cytolytic toxin Cyt1A from *Bacillus thuringiensis* var. *israelensis*. *Biochemistry*. 2005;44:589-597. doi:10.1021/bi048493y
43. Elliott SR. Medium-range structural order in covalent amorphous solids. *Nature*. 1991;354:445-452. doi:10.1038/354445a0

SUPPORTING INFORMATION

Additional supporting information can be found online in the Supporting Information section at the end of this article.

How to cite this article: Chen SW, Teulon J-M, Pellequer J-L. Cry11Aa and Cyt1Aa exhibit different structural orders in crystal topography. *J Mol Recognit*. 2023;36(9):e3047. doi:10.1002/jmr.3047